Mechanical behavior of the membrane during the polymer electrolyte fuel cell operation

Mustafa Fazil Serincan*, Ugur Pasaogullari

Department of Mechanical Engineering, and Center for Clean Energy Engineering, University of Connecticut, 44 Weaver Rd Unit 5233, Storrs, CT, 06269, USA

ABSTRACT

A computational modeling framework is developed to represent the transport phenomena, electrochemistry and the mechanical stresses in a polymer electrolyte fuel cell (PEFC). The model is able to predict the mechanical stresses developed in the polymer electrolyte due to hydration changes, and restriction of the membrane swelling as a result of these hydration changes in the PEFC assembly. Anisotropy in the mechanical properties of the gas diffusion layers is accounted in the stress calculations. It is seen that hydration variations during the PEFC operation can cause significant mechanical stresses. The effects of operating voltage and relative humidities of reactants are investigated. It is observed that high inlet humidities result in a better performance; however, it can potentially cause the polymer electrolyte membrane to go through plastic deformation irreversibly. Thermal stresses due to temperature variations are also calculated and compared with hygral stresses; and it is found that thermal stresses are not negligible but are typically a fraction of the hygral stresses in a typical PEFC operation.

© 2010 Elsevier B.V. All rights reserved.

1. Introduction

Polymer electrolyte membrane fuel cells (PEFCs) are promising candidates for alternative power generation because of their environmental friendly operation and high power densities as well their potential to decrease foreign fuel dependency. The prospect of PEFCs has been demonstrated by numerous applications such as use of these devices in buses, boats, forklifts, backup power systems, etc. ...

Although PEFCs show significant performance results in laboratory conditions, their widespread use in real-life applications depends on the capability of these devices to resist electrochemical and mechanical degradation over time in randomly changing operating environments. Poisoning of the catalyst sites and the membrane due to fuel and air side impurities, loss of active area due to platinum agglomeration and migration, corrosion of the electrodes, and flooding of the electrodes due to poor water management are the most common mechanisms leading to electrochemical degradation of the PEFCs. On the other side, mechanical degradation may be caused by inhomogeneous compression of the membrane-electrode assembly by the bipolar plates; mechanical shock and vibration transmitted to the fuel cell during operation;

thermal hotspots, and mechanical stresses due to swelling of the membrane. For a broader list of degradation mechanisms, we refer to Rama et al. [1].

Mechanical stresses due to swelling of the membrane are studied less than the other factors causing mechanical degradation of the cell. Tang et al. [2] studied the effects of membrane swelling on cell degradation. Tang et al. investigated the mechanical properties of the membrane as a function of humidity of the membrane and its swelling [3,4]. On the other hand, there are a number of computational models to predict the mechanical stresses due to swelling of the membrane [5–9]. However, these studies do not take into account the transport phenomena related to the fuel cell operation. A study by Al-Baghdadi and Al-Janabi incorporates the fuel cell transport phenomena in their structural analysis to predict the effect of operating parameters on the hygro-thermal stresses [9]. Recently Kusoglu et al. [10] developed a model coupling the water transport in a PEFC with the mechanical behavior of the cell.

In our previous study [11], we have presented a model to predict the mechanical stresses induced in polymer electrolyte fuel cell (PEFC) materials during the fuel cell operation due to swelling of the polymer electrolyte membrane (PEM). We have focused on the anisotropy of carbon paper, frequently used as gas diffusion layer (GDL) in a PEMFC, and its impact on the stress distribution in the membrane. Because of the preferential orientation of the fibers in the carbon paper, thermal, electrical and mechanical properties of the GDL show discrepancies in the material plane and through the material plane directions. Indeed, Pasaogullari et al. [12] have studied the role of GDL anisotropy on heat conduction and mass

* Corresponding author. Current address: UNIDO-ICHET, Sabri Ulker Sok. 38/4 Cevizlibag, Zeytinburnu, 34015 Istanbul, Turkey. Tel.: +905325173197; fax: +902124168947.

E-mail address: fazil.serincan@engr.uconn.edu (M.F. Serincan).

Nomenclature

Symbols

a	water activity
c_p	specific heat
c_w	water concentration in the membrane
D	elasticity matrix
D_{jk}	binary diffusivities
D_w	water diffusion coefficient in the membrane
E	Young's modulus
F	Faraday constant
G	shear modulus
i	transfer current density
i_0	exchange current density
$\mathbf{I}$	identity matrix
$\mathbf{J}$	ionic current density vector
h	enthalpy
k	thermal conductivity
K	permeability
M_i	molecular weight
$\mathbf{n}$	surface normal
$\mathbf{N}$	mass flux
n_d	electro-osmotic drag coefficient
p	pressure
Q	volumetric heat source
Q_e	volumetric electronic current source
Q_i	volumetric ionic current source
R	universal gas constant
R_j	volumetric consumption of the jth species
T	temperature
$\mathbf{u}$	velocity vector
U_0	equilibrium voltage
V	inlet velocity
w	species mass fraction
x	species mole fraction

Greek

α	thermal expansion coefficient
$\alpha_{a/c}$	transfer coefficient
β	swelling-expansion coefficient
ε	normal strain
ϕ	potential
γ	shear strain
η	overpotential
φ	porosity
κ	conductivity
λ	membrane water content
μ	dynamic viscosity
ν	Poisson's ratio
ρ	density
σ	normal stress
τ	shear stress

Subscripts

a	anode
c	cathode
D	electro-osmotic drag
e	electronic
eff	effective
el	elastic
eq	equilibrium
f	fluid
i	ionic
j	species
k	species
ref	reference
s	solid
sat	saturation
sw	swelling
th	thermal
eq	equilibrium
T	Transpose
Th	Thermal

diffusion and have shown that the directional properties of the GDL have a significant effect on the temperature and consequently, phase distributions. Regarding the structural behavior of the GDL, Kleemann et al. [13] have studied the anisotropy of the mechanical properties of carbon paper to assess the mechanical integrity of the GDL with neighboring bipolar plates. They have shown that anisotropy of the GDL has a great impact on the clamping forces transmitted from the BPP to the GDL and the membrane which affects the contact resistances between two different layers.

The properties of the orthotropic GDL are measured by Kleemann et al. [13] for Toray TGP-H-060, a common GDL material with a nominal thickness of 190 μm. Due to the orientation of carbon fibers, Toray paper exhibits a very low Young's modulus in the through plane compared to in-plane; the Young's modulus values are 5 MPa and 9 GPa, respectively. As a result when the membrane is swollen the GDL can hardly resist the deformation in through plane direction and the through plane stresses induced in the membrane are negligible compared to the stresses in the material plane. This was a very important observation because till then all the numerical studies predicting the mechanical behavior of the membrane assumed isotropic GDL properties and overestimated the stresses in through plane direction significantly [5–10].

In this work, assuming orthotropic (principal axes of the material coinciding with the coordinate axes) mechanical, electrical and thermal properties of the GDL, we investigate the stress distribution in the membrane during the fuel cell operation. Already having discriminated the effects of the GDL anisotropy, we focus on how the operating conditions affect the structural behavior of the polymer electrolyte membrane. We first investigate the stresses due to the hydration of the membrane at two different operating voltages: 0.7 V as representative for the nominal operating point and 0.4 V as representative for the maximum power operating point. Then we investigate how the relative humidity of the anode and cathode reactants affects the resultant stresses. Finally, we look into the significance of the thermal stresses compared to the hygral stresses in an operating PEFC.

2. Mathematical model

Two complementary models are used in this study: a two-dimensional non-isothermal computational fluid dynamics (CFD) based model to predict the coupled transport phenomena and electrochemical kinetics of the PEFC, and a structural mechanics model that predicts the distribution of mechanical stresses. The two-dimensional model geometry and the subdomains of the model are shown in Fig. 1.

CFD model incorporates coupled mass, species, momentum, heat and charge conservations to describe the operation of the PEFC. Continuity and momentum equations are solved simultaneously in the fluid domains along with the species conservation equations for the gaseous mixtures in the GDLs and the CLs. For water transfer in the polymer electrolyte membrane (PEM), a separate species
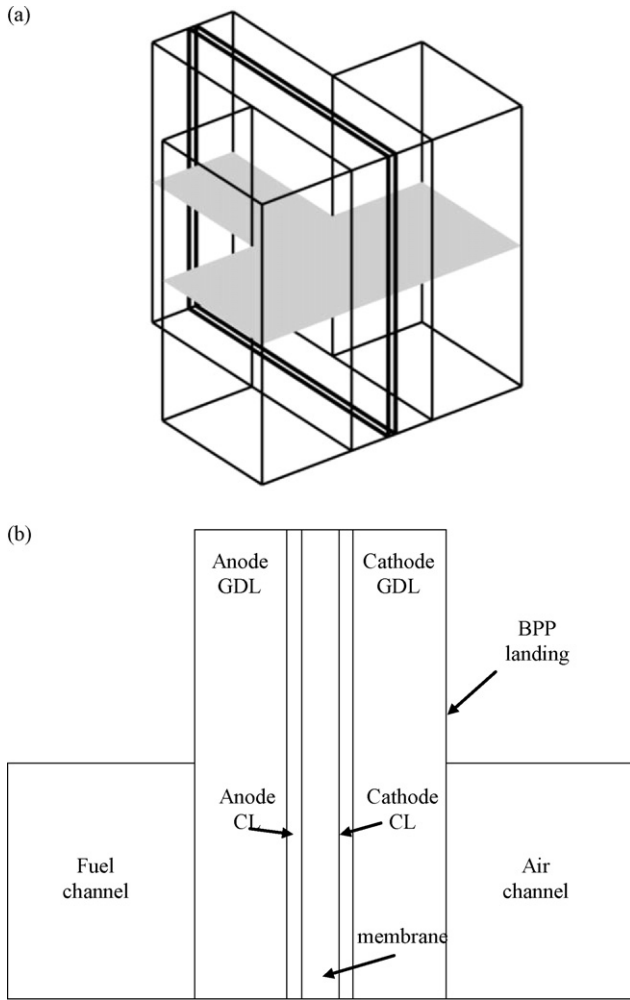
Fig. 1. a) 3D fuel cell geometry. Shaded cross-section is the 2D model geometry. b) Model subdomains are shown on the cross-sectional view. Note that channels are not incorporated in the model, but are shown in the figure for the sake of completeness.

balance is taken into consideration that solves for diffusion and electro-osmotic drag of water. Electronic charge equation is solved in the GDLs and the CLs and ionic charge equation is solved in the CL and the membrane. Energy conservation equation is solved across the entire domain.

Structural mechanics model incorporates the constitutive relations for the isotropic membrane and the CL, and the orthotropic GDL. Orthotropic media is a special form of anisotropic media, where the principal axes of the domain coincide with the principal axes of the coordinate system. Force equilibrium equations in the conservative form are solved in these subdomains to calculate the stresses from the deformation field.

2.1. CFD model

2.1.1. Governing equations
2.1.1.1. Mass and momentum conservation. Continuity equation accounts for mass balance,

$$\nabla \cdot (\rho \mathbf{u}) = 0 \tag{1}$$

where the density of the mixture is calculated as,

$$\rho = \frac{p}{RT} \sum_j x_j M_j \tag{2}$$

Here x_j is the mole fraction of the species determined from the species balance and M_j is the molecular weight of the species. Velocity in Eq. (1) is the superficial velocity and calculated through the Darcy's Law:

$$\mathbf{u} = -\frac{K}{\mu} \nabla p \tag{3}$$

where μ is the dynamic viscosity of the mixture and K is the absolute permeability of the medium.

In the anode and cathode catalyst layers, Eq. (1) is modified to take into account of homogenous reactions and electro-osmotic drag. In the anode catalyst layer, hydrogen is depleted and transformed into H^+, which is absorbed by the ionomer. Also water is adsorbed into the ionomer and transferred through the membrane via electro-osmotic drag. In the cathode, H^+ transferred across the membrane reacts with the O_2 to form water. Also H_2O transferred to the cathode is desorbed into the fluid stream from the ionomer surface. Hence, continuity equation (defined only for the fluid domain) is modified such that in the anode stream, hydrogen (due to electrochemical reaction) and water (due to electro-osmotic drag) is consumed, whereas in the cathode stream water mass is generated and oxygen is consumed. Back-diffusion flux of water from cathode to anode is treated as boundary conditions for the momentum equation as explained in Section 2.1.2. Then appropriate source terms are set in the continuity equation accordingly as $R_a = R_{H_2} - R_{D,H_2O}$ and $R_c = R_{O_2} + R_{H_2O} + R_{D,H_2O}$ for anode and cathode respectively where,

$$R_{H_2} = \frac{-i_a}{(2F)M_{H_2}} \tag{4}$$

$$R_{H_2O} = \frac{i_c}{(2F)M_{H_2O}} \tag{5}$$

$$R_{O_2} = \frac{-i_c}{(4F)M_{O_2}} \tag{6}$$

$$R_{D,H_2O} = \nabla \cdot \left(\frac{n_d}{F} \mathbf{J} \right) M_{H_2O} \tag{7}$$

where n_d is the electro-osmotic drag, F is the Faraday's constant, $\mathbf{J}$ is the ionic current density, and $i_{a/c}$, is the transfer current density at the anode and cathode, as explained in the following sections.

2.1.1.2. Species conservation. Anode and cathode gas mixtures: Multi-component species transport is modeled with Maxwell–Stefan equation in the form developed by Curtis and Bird [14] which can be written for ideal gas mixtures as

$$\nabla \cdot \left[\rho w_j \mathbf{u} - \rho w_j \sum_{k=1}^{n} \tilde{D}_{jk} \left(\nabla x_k + (x_k - w_k) \frac{\nabla p}{p} \right) \right] = R_j \tag{8}$$

which is solved for hydrogen at the anode and oxygen and water at the cathode. Mass fractions of the background species, which are water at the anode and nitrogen at the cathode, are determined via

$$\sum_{j=1}^{n} w_j = 1.$$

In Eq. (8) R_j is the source terms for each species, which are calculated from Eq. (4)–(7). $\tilde{D}_{jk}$ are the Maxwell–Stefan diffusivities and calculated from binary diffusion coefficients. Binary diffusivities are defined as a function of temperature and pressure and then corrected via Bruggemann correlation to account for porosity of the medium [15]

$$D_{jk} = D_{jk}^0(T_0, p_0)\left(\frac{T}{T_0}\right)^{1.5}\frac{p_0}{p}\varphi^{1.5} \tag{9}$$

D_{jk}^0 is the bulk diffusivity measured at T_0 and p_0. φ is the void fraction of the porous medium. Bruggemann correlation assumes that tortuosity of the medium is equal to 1.5 and it appears as the power of φ.

Membrane water transport: Water transport in the membrane is described by the following equation:

$$\nabla \left(D_w \nabla c_w - \frac{n_d}{F} \kappa_i \nabla \phi_i \right) = 0 \tag{10}$$

where the first term represents the water transport due to diffusion and second term represents the water transport due to the electro-osmotic drag. n_d is the electro-osmotic drag coefficient which is taken as unity and D_w is the diffusion coefficient of water given by Motupally et al. [16] as

$$D_w = \begin{cases} 3.1 \times 10^{-7} \lambda (\exp(0.28\lambda) - 1) \exp\left(\frac{-2436}{T}\right) & \text{for } 0 < \lambda \leq 3 \\ 4.17 \times 10^{-8} \lambda (1 + 161 \exp(-\lambda)) \exp\left(\frac{-2436}{T}\right) & \text{for } 3 < \lambda \end{cases} \tag{11}$$

where λ is the effective water concentration in the ionomer that is defined as the number of water molecule per sulfonic acid group:

$$\lambda = \frac{c_w}{c_{SO_3^-}} \quad \text{and} \quad c_{SO_3^-} = \frac{\rho_{mem,dry}}{EW} \tag{12}$$

2.1.1.3. Energy conservation. Steady state heat equation is solved to account for energy balance.

$$\nabla \cdot \left(-k\nabla T + \rho C_p T \mathbf{u} + \sum_j h_j \mathbf{N}_{D,j} \right) = Q \tag{13}$$

Eq. (13) is formulated in the porous regions by volume averaging as described in Ref. [17]. Assuming thermal equilibrium between the gas phase and the solid phase, the volume averaging results in the same form of Eq. (13), with the following modifications: In the porous domains second and third terms are calculated only for the fluid mixture. Porosity corrections are accounted automatically in $\mathbf{u}$ and $\mathbf{N}_{D,j}$, which are the superficial velocity of the mixture and the diffusive flux of each species respectively. Further, an effective thermal conductivity is defined such that and $k_{eff} = \varphi k_f + (1 - \varphi) k_s$ where indices f and s stand for fluid and solid, respectively.

Heat generation during the fuel cell operation is distributed across the MEA to consider reversible and irreversible losses separately in each domain:

$$Q = i_{a/c} \left(\eta + T \frac{dU_{0,a/c}}{dT} \right) + \sigma_i (\nabla \phi_i \cdot \nabla \phi_i) \quad \text{in the CLs}$$
$$Q = \kappa_i (\nabla \phi_i \cdot \nabla \phi_i) \quad \text{in the membrane} \tag{14}$$

where η is the activation overpotential, U_0 is the equilibrium cell potential, σ_i is the ionic conductivity of the membrane, ϕ_i is the ionic phase potential as described in the next section. Here, we assume that ohmic loss due to electron transfer is negligible compared to the other contributions to the heat source. In this model, the heat generation due to contact resistance between the components is also assumed to be negligible.

2.1.1.4. Charge conservation. Electronic and ionic charge conservations are:

$$-\nabla \cdot (\kappa_e \nabla \phi_e) = j \tag{15}$$

$$-\nabla \cdot (\kappa_i \nabla \phi_i) = -j \tag{16}$$

Ionic charge conservation equation is solved in the ionically (proton) conductive CLs and the membrane whereas electronic charge conservation equation is solved in the electronically conductive GDLs and the CLs. Ionic conductivity of the membrane is

Table 1
Material properties.

Gas diffusion layers		
Porosity	0.78	[24]
Through-plane electronic conductivity ($S\,m^{-1}$)	12.5	[24]
In-plane electronic conductivity ($S\,m^{-1}$)	172.4	[24]
Through-plane thermal conductivity ($W\,m^{-1}\,K^{-1}$)	1.7	[24]
In-plane thermal conductivity ($W\,m^{-1}\,K^{-1}$)	23	[24]
Hydraulic permeability (m^2)	2e12	[20]
Through-plane Young's modulus (MPa)	$E_x = f(\varepsilon_x)^a$	[13]
In-plane Young's modulus (MPa)	9000	[13]
Poisson's ratio in xy plane	0	[13]
Poisson's ratio in yz plane	0.25	[24]
Shear modulus in xy plane (MPa)	19.5	[13]
Thermal expansion coefficient (K^{-1})	-0.8×10^{-6}	[24]
Density ($kg\,m^{-3}$)	440	[24]
Catalyst layers		
Porosity	0.2	b
Ionomer volume fraction	0.26	[20]
Thermal conductivity ($W\,m^{-1}\,K^{-1}$)	0.87	b
Hydraulic permeability (m^2)	2e12	b
Density ($kg\,m^{-3}$)	2100	b
Anode exchange current density ($A\,m^{-3}$)	3×10^9	b
Cathode exchange current density ($A\,m^{-3}$)	3×10^4	b
Anodic and cathodic transfer coefficients at the anode	$\alpha_a = \alpha_c = 1$	[20]
Cathodic transfer coefficients at the anode	$\alpha_c = 1$	[20]
Membrane		
Thermal conductivity ($W\,m^{-1}\,K^{-1}$)	0.259	[24]
Young's modulus (MPa)	$E = f(\lambda, T)^a$	[7]
Poisson's ratio	0.25	[24]
Thermal expansion coefficient (K^{-1})	123×10^{-6}	[24]
Density ($kg\,m^{-3}$)	1980	[24]
Equivalent weight (EW)	1100	[24]

a See the text.
b Assumed values.

given as a function of water content via the following expression [18]

$$\kappa_i = (0.5139\lambda - 0.326) \exp\left[1268 \left(\frac{1}{303} - \frac{1}{T} \right) \right] \tag{17}$$

Source terms in charge conservation equations are the rate of charge transfer. $j = i_a$ at the anode and $j = i_c$ at the cathode. Electrochemical kinetics of anode and cathode are described via the linear kinetics (due to sufficiently fast) and Tafel kinetics (due to sufficiently slow) approximations to the Butler–Volmer equation in the anode and cathode, respectively: [19].

$$i_a = i_{0,a} \left(\frac{x_{H_2}}{x_{H_2}^{ref}} \right)^{1/2} \left(\frac{\alpha_a + \alpha_c}{RT} F\eta_a \right) \tag{18}$$

$$i_c = i_{0,c} \left(\frac{x_{O_2}}{x_{O_2}^{ref}} \right) \exp\left(-\frac{\alpha_c}{RT} F\eta_c \right) \tag{19}$$

$i_{0,a/c}$ are the exchange current densities and $\alpha_{a/c}$ are the reaction transfer coefficients for the anode and the cathode. Values are listed in Table 1. Activation overpotential, η, is defined as:

$$\eta_{a/c} = \phi_e + \phi_i - U_{0,a/c} \tag{20}$$

where equilibrium voltage $U_{0,a/c}$ are defined as [20]

$$U_{0,a} = \begin{cases} 0 & \text{at the anode} \\ 1.23 - 9 \times 10^{-4}(T - 298.15) & \text{at the cathode} \end{cases} \tag{21}$$

2.1.2. Boundary conditions

2.1.2.1. Maxwell–Stefan equations.
Species mass fractions are fixed at the fuel channel inlet and the outer cathode boundaries,

$$w_j = w_{j,\text{in}} \tag{22}$$

At the fuel channel outlet, convective flux boundary condition is imposed to indicate there is no diffusion related mass transfer through this boundary.

$$\mathbf{n} \cdot \left[-\rho w_j \sum_{k=1}^{n} \tilde{D}_{jk} \left(\nabla x_k + (x_k - w_k)\frac{\nabla p}{p} \right) \right] = 0 \tag{23}$$

Note that, in the Maxwell–Stefan equations H_2O is designated as the background species in the anode. Therefore, boundary conditions are only prescribed for H_2. If Dirichlet type boundary conditions are specified for H_2, the boundary conditions for H_2O are determined via the expression $\sum_{j=1}^{n} w_j = 1$. On the other hand if Neumann type boundary conditions are specified for H_2 then the ones for H_2O are determined through the continuity using the boundary conditions specified for the momentum equation.

2.1.2.2. Water transport in the membrane.
In the catalyst layer membrane interfaces local equilibrium between the gas phase and the ionomer phase is assumed and boundary conditions are given as

$$c_\text{w} = c_\text{w}^\text{eq} \tag{24}$$

where equilibrium value is determined by Eq. (12) and the water sorption isotherms, given as a relation between the membrane water content and the local water activity $a = p_\text{w}/p_\text{sat}$

$$\lambda = 0.3 + 6a[1 - \tan h(a - 0.5)] + 3.9\sqrt{a}\left[1 + \tan h\left(\frac{a - 0.89}{0.23}\right)\right] \tag{25}$$

Above relation is given by Kulikovsky [21] as a curve fit to Hinatsu et al.'s [22] experiments to characterize water uptake of Nafion at 80 °C.

2.1.2.3. Momentum conservation.
Pressure boundary conditions are prescribed for Darcy's Law at the GDL-channel interfaces. The other boundaries are treated with symmetry conditions. At the CL membrane interfaces special attention is required to model the water transport. At the CL – membrane interface, water transferred through the membrane either enters or leaves the fluid domain with a superficial velocity which can be calculated from the mass balance.

$$\rho V = -\mathbf{n} \cdot (-D_\text{w}\nabla c_\text{w})M_{H_2O} \tag{26}$$

where right hand side is the mass flux calculated by water transport equation at the normal direction of the interface. The negative sign in front of the normal vector $\mathbf{n}$ implies that the calculated mass flux is through the membrane. Therefore for the momentum equation V is specified as outlet velocity at the CL – membrane boundaries.

2.1.2.4. Energy conservation.
At the flow inlets, fixed temperature is assumed as well as at the interfaces between the channels and the bipolar plates. The latter assumption derives from the large thermal conductivity of the bipolar plates and the thermal mass of the coolant at the controlled temperature.

At the outlet of the fuel channel; boundary conditions are set as convective flux, which means any heat transport through that boundary is convection dominated and there is no heat flux due to conduction. The rest of the boundaries are treated as insulation/symmetry planes.

2.1.2.5. Charge conservation equations.
For ionic charge conservation all boundary conditions are set to insulation,

$$\mathbf{n} \cdot (\kappa_\text{i}\nabla\phi_\text{i}) = 0 \tag{27}$$

For electronic charge conservation, voltage boundary condition at the cathode GDL – bipolar plate interface and ground at the anode GDL – bipolar plate interface are prescribed. This implies the assumption of infinitely conductive bipolar plates. The rest of the boundaries are treated as insulation.

2.2. Structural mechanics model

2.2.1. Constitutive relations
In this study we use plane strain assumption due to the high aspect ratio of the fuel cell geometry, i.e., channel length 50 mm and the total thickness of the MEA is 0.5 mm. It is also assumed that GDLs, CLs and the membrane undergo linear deformation when subject to hygro-thermal loading. The total strain consists of elastic, hygral, thermal strain components:

$$\varepsilon = \varepsilon_\text{el} + \varepsilon_\text{sw} + \varepsilon_\text{th} \tag{28}$$

With the assumption that hygral and thermal expansions are isotropic, the total strain becomes:

$$\varepsilon = \begin{bmatrix} \varepsilon_x \\ \varepsilon_y \\ 0 \\ \gamma_{xy} \end{bmatrix} + \begin{bmatrix} \varepsilon_\text{sw} \\ \varepsilon_\text{sw} \\ \varepsilon_\text{sw} \\ 0 \end{bmatrix} + \begin{bmatrix} \varepsilon_\text{th} \\ \varepsilon_\text{th} \\ \varepsilon_\text{th} \\ 0 \end{bmatrix} \tag{29}$$

Hygral and thermal strains in normal directions are calculated as

$$\varepsilon_\text{sw} = \beta(c_\text{w} - c_\text{w,ref}) \tag{30}$$

$$\varepsilon_\text{th} = \alpha(T - T_\text{ref}) \tag{31}$$

where β is the membrane swelling-expansion coefficient (SEC) defined as change in length for 1% change in relative humidity and α is the thermal expansion coefficient (TEC). c_w, water content and T, temperature field are taken from the solution of the CFD model. $c_\text{w,ref}$, and T_ref are the values for stress free states (i.e., zero stress state) for hygral and thermal expansions respectively. In the simulations we assume that before the assembly, Nafion 112 membrane is initially hydrated at a 30% relative humidity environment, which corresponds to the stress free state for hygral expansion. Considering that the cell is assembled at room temperature, the stress free state for thermal expansion is taken as 25 °C.

Stress–strain relationship for a linear elastic material is given by:

$$\sigma = D\varepsilon_\text{el} \tag{32}$$

which can be rewritten using Eq. (28) as

$$\sigma = D(\varepsilon - \varepsilon_\text{sw} - \varepsilon_\text{th} - \varepsilon_0) \tag{33}$$

Components of σ are σ_x, σ_y, σ_z, τ_{xy} which are the normal and the shear stresses. In this study we model the GDL and the CL as orthotropic materials and the membrane is assumed to be isotropic. For an isotropic material the compliance matrix, the inverse of D, is defined as

$$D^{-1} = \frac{1}{E} \begin{bmatrix} 1 & -\nu & -\nu & 0 \\ -\nu & 1 & -\nu & 0 \\ -\nu & -\nu & 1 & 0 \\ 0 & 0 & 0 & 2(1+\nu) \end{bmatrix} \tag{34}$$

where E is the Young's modulus and ν is the Poisson's ratio of the material. On the other hand, for an orthotropic material the compliance matrix is defined as following:

$$D^{-1} = \begin{bmatrix} 1/E_x & -\nu_{xy}/E_y & -\nu_{zy}/E_z & 0 \\ -\nu_{xy}/E_x & 1/E_y & -\nu_{yz}/E_z & 0 \\ -\nu_{zy}/E_x & -\nu_{yz}/E_y & 1/E_z & 0 \\ 0 & 0 & 0 & 1/G_{xy} \end{bmatrix} \quad (35)$$

where E needs to be known in three normal directions and ν and G, the shear modulus, need to be determined in three different shear planes. Unlike in the case of isotropic materials, these three moduli are not coupled and shear modulus has to be determined separately. However, considering the morphology of the carbon fiber GDLs, it is observed that the fibers are aligned parallel to the material plane, but without having an in-plane preferential orientation. Therefore we assume isotropic in-plane (yz plane) properties which implies $E_y = E_z$, $\nu_{xy} = \nu_{xz}$.

2.2.2. Material properties
2.2.2.1. Membrane.
Tang et al. determined the swelling strain and Young's modulus of Nafion 112 as a function of relative humidity and temperature [3]. The polynomial fit to their strain vs. relative humidity data and the Young's modulus values for different relative humidities can be found in Ref. [7]. In our work we relate these properties to the membrane water content since we predict water content rather than relative humidity in the membrane. A curve fit to the experimental swelling strain data at 85 °C results in:

$$\varepsilon_{sw} = 0.02154 \times \lambda - 0.051846 \quad (36)$$

Another curve fit to their Young's modulus data at 85 °C results in ($R^2 = 0.99$):

$$E = 28.14 \times \exp(3.665\lambda) \quad (37)$$

where Young's modulus is in MPa.

TEC and Poisson's ratio of the Nafion 112 are determined from the product data sheet [23]. The values are listed in Table 1.

2.2.2.2. Gas diffusion layers.
The in-plane and through plane mechanical properties for Toray TGP-H-060 GDL has been investigated by Kleemann et al. [13]. They report the values for through plane and in-plane Young's moduli (E_x, E_y), Poisson's ratio in the xy plane (ν_{xy}), and the shear modulus in the xy plane (G_{xy}). The values are listed in Table 1 except for E_x, which is not a constant but is given as a function of through plane strain. After carrying out a curve fit to their data, through plane Young's modulus is expressed as (in MPa) (Table 1):

$$E_x = 89.427 \times \varepsilon_x^2 + 2.5816 \times \varepsilon_x + 0.51926 \quad (38)$$

Poisson's ratio in the material plane (ν_{yz}) as well as the TEC of the GDL is taken from the product data sheet [24].

2.2.2.3. Catalyst layers.
The catalyst layers consist of ionomer and packed carbon particles. It is assumed that catalyst layer elastic properties are determined by the membrane phase therefore membrane properties are used for the CLs.

2.2.3. Boundary conditions
The assembly of GDL, CL and membrane is constrained with the bipolar plates (BPP) at both sides. The boundary conditions at the GDL–BPP interfaces are chosen such that motion is constrained in all three directions. At the GDL–channel interfaces the assembly is assumed to be deforming freely. The rest of the boundaries are treated as symmetry planes. Geometrical parameters are given in Table 2.

Table 2
Geometrical and operational parameters.

|	
Fuel and air channel width	0.5 mm
Fuel and air channel depth[a]	0.5 mm
Land area width	0.5 mm
GDL thickness	0.2 mm
CL thickness	10 μm
Membrane thickness (Nafion 112)	50.8 μm
GDL, CL and membrane depth[a]	1 mm
Fuel and air channel, GDL, CL and membrane length	50 mm
Anode and cathode inlet relative humidity	30/30%
Operating temperature (°C)	80
Anode and cathode back-pressure (atm)	1

[a] Half of the actual depth is considered due to symmetry of the geometry.

3. Results

3.1. Effect of operating voltage

Fig. 2 shows the deformation of the fuel cell structure comprised of anode gas diffusion layer (GDL) and catalyst layer (CL), membrane and cathode CL and GDL at (a) 0.7 V and (b) 0.4 V. The inlet relative humidities in both sides are taken as 50%. It is seen that the GDL deforms through the channel while it is restricted at the upper half by the bipolar plate landings. There is a little difference seen in the deformations between two voltages, however, it can be seen that the deformation of the membrane for the fuel cell operating at 0.4 V is slightly greater. At 0.4 V membrane water content is higher due to larger current generation, therefore the swelling of the membrane due the change in hydration compared to stress free state is higher.

Another distinction between these two figures is that at 0.7 V the deformation of the membrane is uniform at the cathode side whereas at 0.4 V the membrane deforms more at the upper half (under the current collector rib). The path for removal of generated water to the channels is longer from under the rib areas compared to from under the channel areas. As a result, more water is accumulated under the rib areas causing the membrane to swell more. At lower voltages this non-uniformity is more notable because more water is accumulated under the rib areas due to the increased water generation. It can be seen in Fig. 3 that at 0.7 V the water content in the cathode CL is changing from 3.65 under the rib areas to 3.5 under the channel areas, while at 0.4 V the water content is 4.16
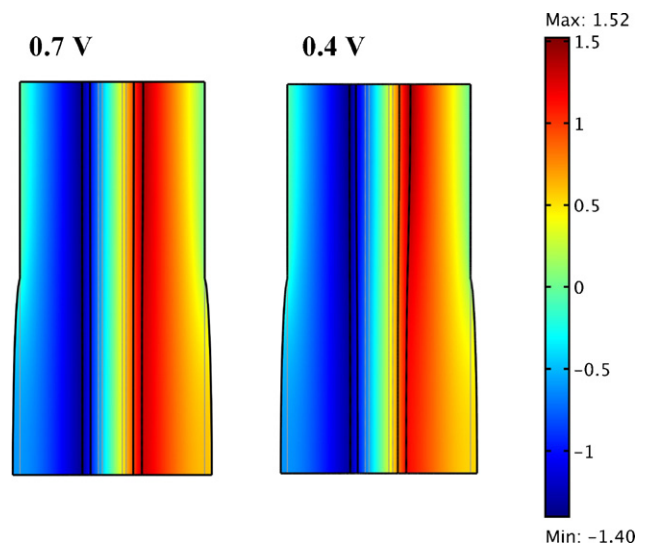

Fig. 2. Displacement fields (μm) and the deformation during the fuel cell operation at 0.7 and 0.4 V with anode and cathode inlet relative humidities as 50/50%. Gray lines show undeformed geometry.
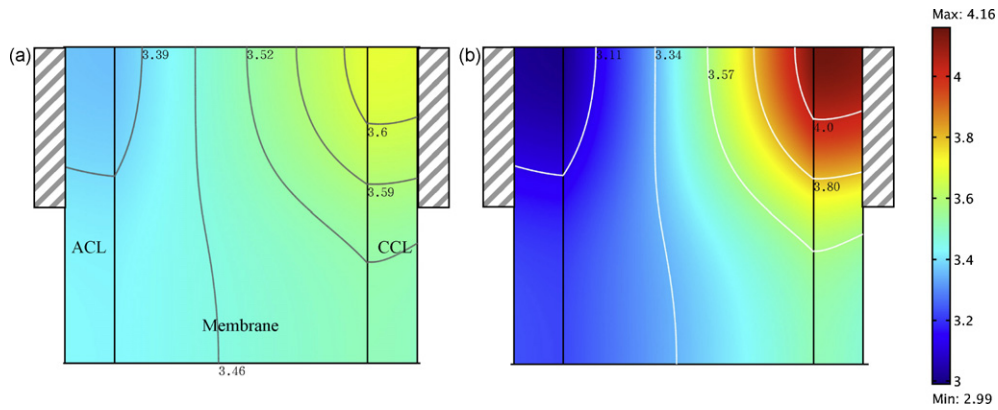
Fig. 3. Water content distribution in the membrane-electrode assembly (anode catalyst layer, membrane and cathode catalyst layer) for the fuel cell operating at a) 0.7 V, b) 0.4 V with anode and cathode inlet relative humidities as 50/50%. Hatched blocks represent the bipolar plate landings.
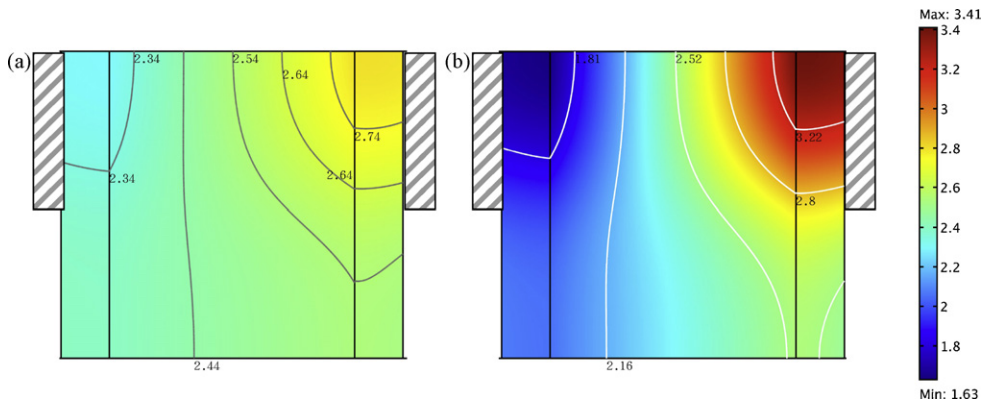
Fig. 4. In-plane compressive stress distributions (MPa) during fuel cell operation at a) 0.7 V, b) 0.4 V. In comparison, Tang et al. [3] measured the yield strength of Nafion 112 to be between 2.29 and 6.60 MPa in a temperature and relative humidity range of 25–85 °C and 30–90% relative humidity.
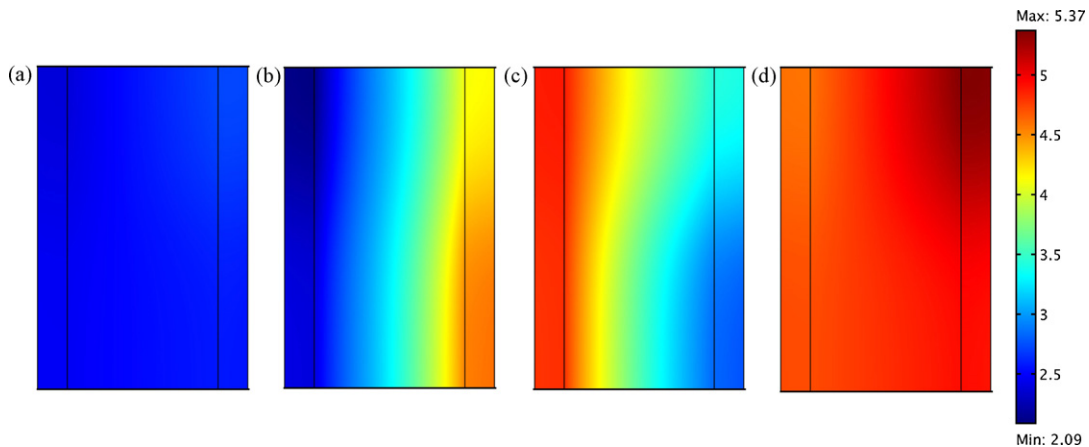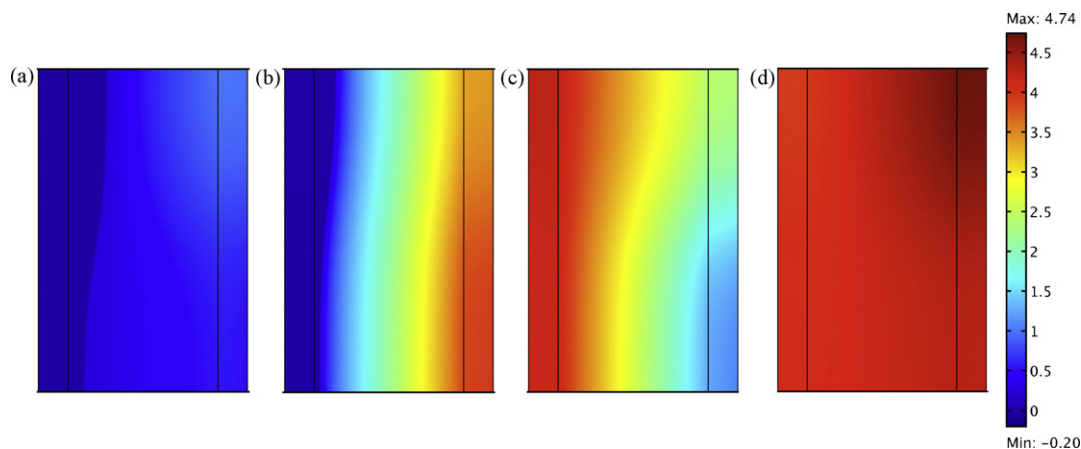

Fig. 5. Membrane water content distributions for the fuel cell operating at 0.7 V with anode and cathode relative humidities of a) 30/30%, b) 30/70%, c) 70/30%, and d) 70/70%. Cell operating temperature is 80 °C.

at under the rib and 3.4 at under the channel areas. The in-plane variation in the water content is not significant at 0.7 V compared to that at 0.4 V. As a result, deformation is uniform at the cathode GDL interface.

It is also observed in Fig. 2 that the deformation of the membrane-electrode assembly (MEA) is not symmetric but the displacements are greater at the cathode side because of larger water content in the cathode side of the membrane. The maximum through plane displacement at the cathode side is observed as 1.52 μm at under the rib areas for the fuel cell operating

at 0.4 V while the maximum displacement at the anode side is 1.40 μm.

In-plane compressive stresses for the fuel cell operating at 0.7 and 0.4 V are seen in Fig. 4. Consistent with the water content distribution in the membrane and the catalyst layers, the biggest stresses occur under the rib areas. The magnitude of the stresses in compression reaches up to 2.8 and 3.4 MPa for 0.7 and 0.4 V respectively. In-plane compressive stresses occur in the membrane because the GDL constrains the swelling of the membrane due to the larger difference between in-plane Young's moduli of two layers. In com-

Fig. 6. In-plane compressive stress distributions (MPa) for the fuel cell operating at 0.7 V with anode and cathode relative humidities of a) 30/30%, b) 30/70%, c) 70/30%, and d) 70/70%. Cell operating temperature is 80 °C.

parison, Tang et al. [4] measured the yield strength of Nafion 112 to be between 2.29 and 6.60 MPa in a temperature and relative humidity range of 25–85 °C and 30–90% relative humidity. On the other hand through-plane Young's moduli of GDL and the membrane are comparable. Thus, the motion of the membrane due to swelling is hardly restricted by the GDL. As a result through-plane stresses are negligible compared to in-plane stresses, since they are only in the order of 5 kPa.

3.2. Effect of relative humidity of the inlet gases

Fig. 5 shows the water content in the membrane and the catalyst layers for the fuel cell operating at 0.7 V with anode and cathode inlet relative humidities of 30/30%, 30/70%, 70/30% and 70/70% at 80 °C. In the 30/30% case, the net water transport coefficient is positive, therefore there is a net water transport from anode to cathode since the back-diffusion is not able to compensate for electro-osmotic drag, and water content decreases at the anode side. Based on the swelling strain data of Tang et al. [4], it is assumed that the fuel cell is assembled when the membrane is initially humidified at 30%. Corresponding membrane water content (λ) at 80 °C is calculated to be 2.408. For the first two cases when the anode inlet relative humidity is 30%, membrane water content decreases as low as $\lambda = 2$, lower than the initial membrane water content. Thus, membrane does not swell but shrink where the water content is lower than its initial assembly value.

Correspondingly, as seen in Fig. 6 at these regions tensile stresses occur because they are *pulled* by the swollen membrane. Tensile stresses as high as 0.2 MPa are observed for the first two cases. The region of tensile stresses is larger for the first case, when both anode and cathode inlet relative humidities are 30%, than for the second case, when anode and cathode inlet relative humidities are 30/70%. This is because of the increased water content at the anode side due to the back diffusion from cathode to anode. Back diffusion is more notable for the second case due to the higher cathode relative humidity.

In the third case, when the inlet relative humidities of the anode and cathode are 70% and 30%, respectively, membrane water content is as high as $\lambda = 5$. Corresponding compressive stresses are higher at the anode side and under the rib areas. At the anode catalyst layers, compressive stresses as high as 4.5 MPa are observed.

For the last case when both anode and cathode inlet relative humidities are 70% a more homogenous water content distribution is observed, with λ between 4.5 and 5.4. Increased membrane water content implies greater ionic conductivity and a better electrochemical performance. However, corresponding compressive stresses are between 4 and 4.75 MPa whereas the yield strength of the membrane is 3 MPa at 85 °C. It should be noted that the yield strength is a function of membrane water content and temperature. Tang et al. [4] measured yield strength of the membrane for different membrane water contents. For membrane water content of 2.48, 3.48, 4.72 and 7.51 yield strength of the membrane is reported
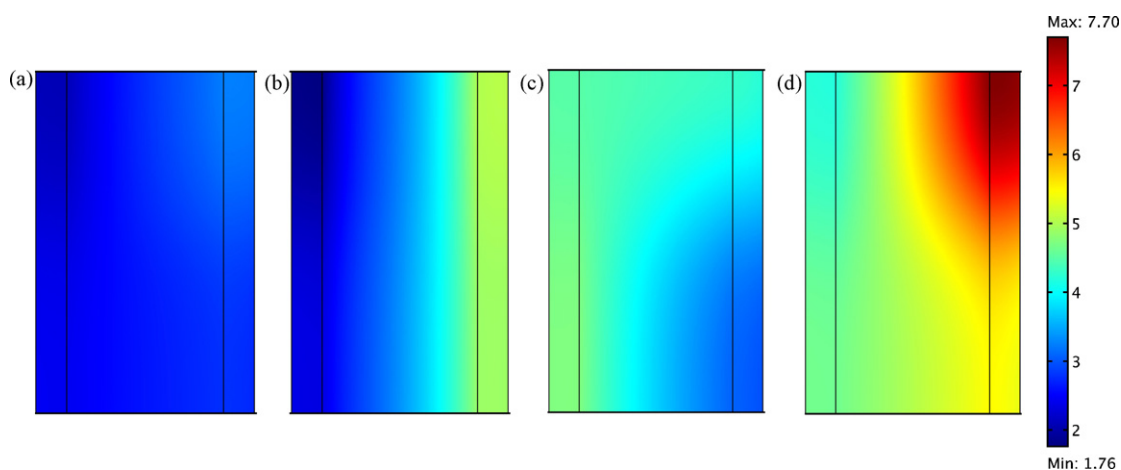
Fig. 7. Membrane water content distribution for the fuel cell operating at 0.7 V with anode and cathode relative humidities of a) 30/30%, b) 30/70%, c) 70/30%, and d) 70/70%. Cell operating temperature is 80 °C.
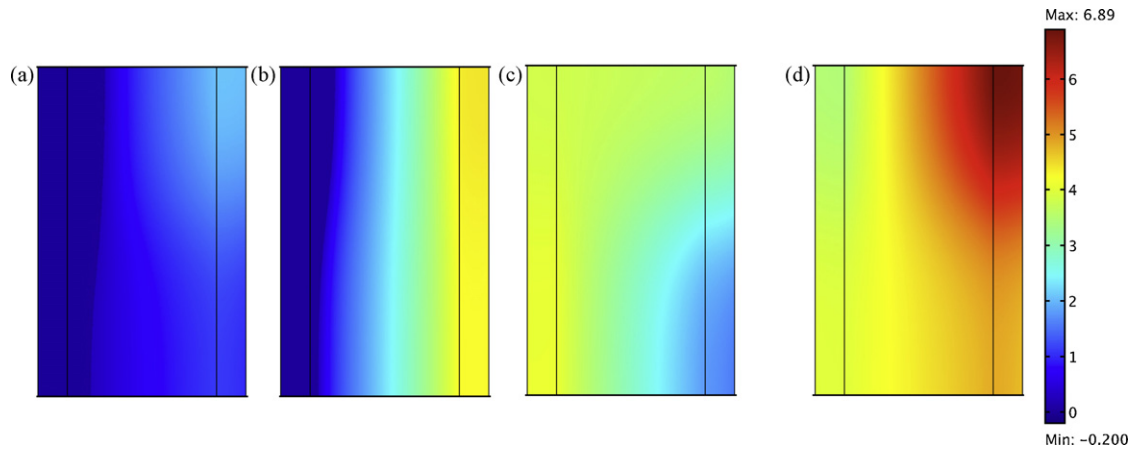
Fig. 8. In-plane compressive stress distributions (MPa) for the fuel cell operating at 0.7 V with anode and cathode relative humidities of a) 30/30%, b) 30/70%, c) 70/30%, and d) 70/70%. Cell operating temperature is 80 °C.

to be 3.61, 3.44, 3.08 and 2.20 MPa, respectively. Increase in membrane water content decrease the strength of the membrane.

Considering Figs. 5 and 6 along with the above data, it is predicted that for the first case the deformation of the membrane is in the elastic region as the compressive stresses stay well below the yield limit. In the second case when the cathode relative humidity increases to 70% the compressive stresses goes slightly above the yield strength in areas of the cathode CL under the gas channel. In the third case when the anode and cathode relative humidities are 70/30% half of the membrane closer to anode side experience stresses above yield strength. Finally in the last case, when both anode and cathode relative humidities are 70% almost the entire membrane exceeds the yield strength. Note that our model assumes linear elastic deformations and is not capable of predicting the mechanical behavior in the plastic region of the stress–strain curve. These predictions, however, suggest that under some conditions there is a chance that the membrane undergoes plastic deformations. Predicting the membrane behavior in plastic region is an ongoing study of our group.

Fig. 7 shows the water content in the membrane and the catalyst layers for the fuel cell operating at 0.4 V with anode and cathode inlet relative humidities of 30/30%, 30/70%, 70/30% and 70/70%.

Fig. 8 shows the corresponding in-plane compressive stresses. At 0.4 V, current density is higher and more water is generated at the cathode. On the other hand, electro-osmotic drag also increased as it is linearly related to current density. Considering these two effects together, membrane water content is expected to decrease at the anode and to increase at the cathode when compared to the distribution at 0.7 V.

For the first two cases, membrane water content is as low as 1.76 at the anode side which is 15% lower than the value at 0.7 V. As a result of this drop, the regions of the membrane where tensile stresses occur get slightly bigger. For the second case the compressive stresses increase up to 4.2 MPa at the cathode side which is above the yield strength of 3 MPa. Comparing Figs. 6b and 8b it is observed that the chances of the membrane to undergo plastic deformations get bigger for the second case.

For the third case, when anode and cathode relative humidities are 70/30%, it is observed that the membrane water content is more uniform at 0.4 V as more water is dragged from anode to cathode. This alleviates the stress distribution a little bit but it is predicted that there is still possibility for the membrane to undergo plastic deformation. For the last case it is observed that more water is accumulated in the cathode at 0.4 V. λ increases up to 7.7 while the corresponding compressive stresses increase up to 6.9 MPa which is well above the yield strength.
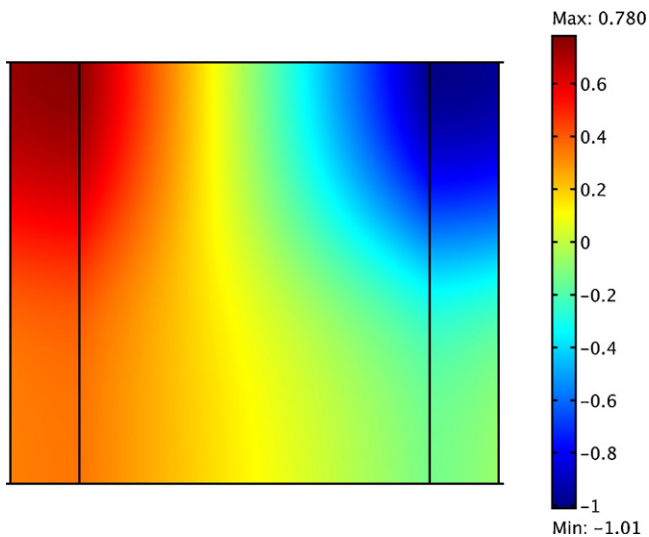
Fig. 9. The difference in compressive stresses (MPa) between those caused by nonuniform membrane water content (at 0.4 V with 50/50% inlet relative humidities) and constant membrane water content (Water content in the latter is the average of the one in the former case).
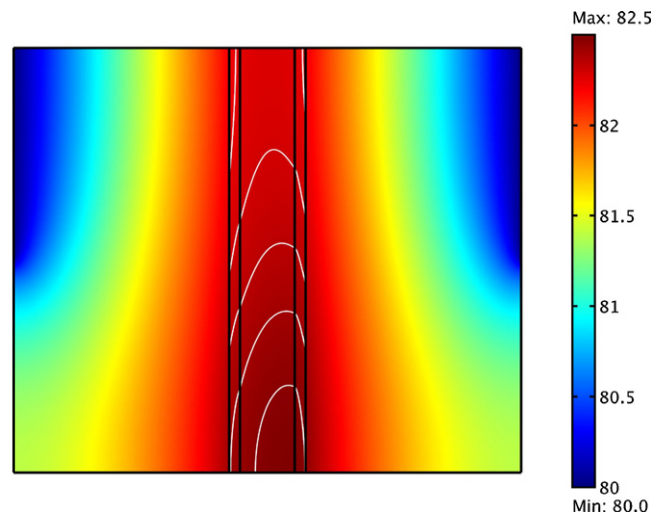
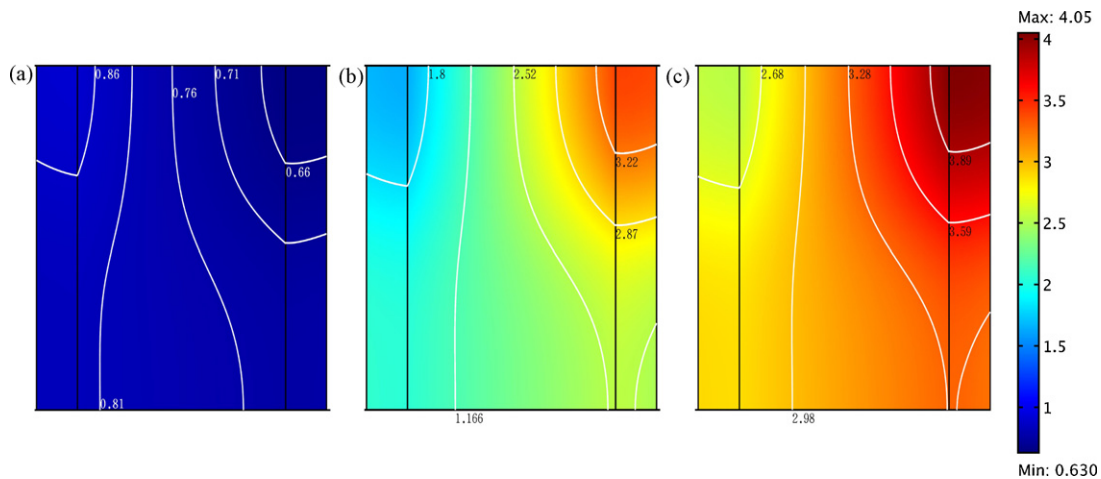**Fig. 10.** Temperature distribution (°C) for the fuel cell operating at 0.4 V.

Fig. 11. Compressive stress distribution (MPa) at 0.4 V. a) thermal stresses, b) hygral stresses, c) combination of both.

3.3. Effect of water content gradient

As a result of swelling, hygral stresses may be induced in the membrane due to either the difference in mechanical properties between the neighboring layers or non-linear gradients in the membrane water content. To investigate the impact of the gradients on the resultant stress distribution, we simulate a case when membrane water content λ is constant. The difference in stresses between the actual case when the membrane water content is nonuniform and the case when λ is constant is attributed to the effect of water content gradients.

For the fuel cell operating at 0.4 V with anode and cathode relative humidities of 50/50%, the difference in the stress distribution between those caused by the nonuniform membrane water content and the constant membrane water content is shown in Fig. 9. The constant λ is taken as the average of the membrane water content for the actual case. (Recall the water content and corresponding stress distributions for the 50/50% inlet relative humidities which are shown in Figs. 3b and 4b). For the hypothetical case of uniform water content, compressive stresses are predicted to be almost constant at 2.41 MPa.

Typically, water content in the cathode side is higher than the average water content due to water production and lower in the anode side due to net water transport. Thus, in case of a water content distribution as seen in Fig. 3b, greater compressive stresses exist at the cathode side. Consistently as seen in Fig. 9 the effect of the water content gradient is that the compressive stresses increase at the cathode sides and decrease at the anode side. Assuming anode side does not go through extreme tension, this would mean that mechanical failure of the membrane initiates on the cathode side, unless it is augmented by any other factors such as chemical decomposition.

3.4. Comparison of thermal stresses with hygral stresses

In addition to swelling, stresses can also be induced in the MEA due to the difference in thermal expansion behaviors of neighboring layers. Similar to the hygral stresses, thermal stresses are also related to the assembly conditions. If the fuel cell is assembled at room temperature and operated at 80 °C, then the thermal strain of the membrane can be calculated as $\varepsilon_{th} = 125 \times 10^{-6} \times (80{-}25) = 0.0069$. On the other hand, the swelling strain can be calculated via

$$\varepsilon_{sw} = 0.02154 \times \lambda - 0.051846$$

For even a very low membrane water content of $\lambda = 4$, the swelling strain is calculated as $\varepsilon_{sw} = 0.0343$. For a typical fuel cell operation, membrane water content will be higher, so will the swelling strain. Hence, thermal stresses are not negligible but are not as large in magnitude as hygral stresses in a PEFC. Nevertheless, in the final section of our analyses, we will investigate how important the thermal stresses are when compared to the mechanical stresses during the fuel cell operation.

Fig. 10 shows the temperature distribution for the fuel cell operating at 0.4 V with 50/50% inlet relative humidities. We predict a maximum temperature increase of 2.5 °C due to heat generation during fuel cell operation (in Eq. (13) $Q = (E_{tn} - V_{cell})I$). The contours are also plotted in the membrane to detail the temperature distribution inside the MEA. Since cathode activation losses are greater, the rise in temperature is also larger at the cathode.

Fig. 11a shows the compressive thermal stresses induced in the MEA due to the temperature distribution seen in Fig. 10. Hygral stresses in the MEA for the same case are seen in Fig. 11b while Fig. 11c shows the resultant net stress distribution. When the first two figures are compared, it is seen that at the anode where the membrane water content is as low as $\lambda = 3$, the thermal stresses are comparable to hygral stresses. On the other hand at the cathode when λ is as high as 4.16 the hygral stresses are much more significant.

4. Conclusions

Stresses developed in the polymer electrolyte membrane during operation of a polymer electrolyte fuel cell are investigated. Mechanical stresses in the membrane are caused by the restriction of its swelling by the GDL and cell assembly. Typical GDL substrates (e.g., carbon paper) show strong anisotropy due to preferential orientation of fibers. Due to the very low Young's modulus of the GDL in through plane direction (anode to cathode) compared to its in-plane value, the through plane stresses become negligible as the GDL does not constrain the swelling of the membrane in through plane direction, but significant stresses develop in the in-plane direction. Effects of operating voltage and relative humidity of the inlet gases are outlined. It is observed that although high inlet humidities result in better electrochemical performance, the hygral stresses developed in the membrane in high humidity conditions are larger and it can potentially lead the fuel cell membrane to deform irreversibly as the in-plane stresses induced in the membrane during fuel cell operation exceeds the yield strength. It is predicted that in case of a failure due to the hygral stresses, cathode

side is more vulnerable. Moreover, thermal stresses are compared with the hygral stresses and it is found that thermal stresses are not negligible but is only a fraction of the hygral stresses in a typical fuel cell operation.

Acknowledgements

References

[1] P. Rama, R. Chen, J. Andrews, in: Proceedings of the Institution of Mechanical Engineers, Part A, J. Power Energy 222 (2008) 421.
[2] H. Tang, S. Peikang, S.P. Jiang, F. Wang, M. Pan, J. Power Sources 170 (2007) 85.
[3] Y. Tang, A.M. Karlsson, M.H. Santare, M. Gilbert, S. Cleghorn, W.B. Johnson, Mater. Sci. Eng. A 425 (2006) 297.
[4] Y. Tang, A. Kusoglu, A.M. Karlsson, M.H. Santare, S. Cleghorn, W.B. Johnson, J. Power Sources 175 (2008) 817.
[5] A. Webber, J. Newman, AIChE J. 50 (2004) 3215.
[6] D. Bograchev, M. Gueguen, J.C. Grandidier, S. Martemianov, Int. J. Hydrogen Energy 33 (2008) 5703.
[7] A. Kusoglu, A.M. Karlsson, M.H. Santare, S. Cleghorn, W.B. Johnson, J. Power Sources 161 (2006) 987.
[8] A. Kusoglu, A.M. Karlsson, M.H. Santare, S. Cleghorn, W.B. Johnson, J. Power Sources 170 (2007) 345.
[9] M.A.R.S. Al-Baghdadi, H.A.K.S. Al-Janabi, Int. J. Hydrogen Energy 32 (2007) 4510.
[10] A. Kusoglu, M.H. Santare, A.M. Karlsson, S. Cleghorn, W.B. Johnson, J. Electrochem. Soc. 157 (2010) B705.
[11] M.F. Serincan, U. Pasaogullari, J. Power Sources 196 (2011) 1314–1320.
[12] U. Pasaogullari, P.P. Mukherjee, C.Y. Wang, K.S. Chen, J. Electrochem. Soc. 154 (2007) B823.
[13] J. Kleemann, F. Finsterwalder, W. Tillmetz, J. Power Sources 190 (2009) 92.
[14] C.F. Curtiss, R.B. Bird, Ind. Eng. Chem. Res. 38 (1999) 2515.
[15] R.E. De La Rue, C.W. Tobias, J. Electrochem. Soc. 106 (9) (1959) 827.
[16] S. Motupally, A.J. Becker, J.W. Weidner, J. Electrochem. Soc. 147 (2000) 3171.
[17] A. Faghri, Y. Zhang, Transport Phenomena in Multiphase Systems, Academic Press – Elsevier Inc., Burlington, MA, 2006.
[18] T.E. Springer, T.A. Zawodinski, S. Gottesfeld, J. Electrochem. Soc. 136 (1991) 2334.
[19] J.M. Bockris, A.K.N. Reddy, Modern Electrochemistry, vol. 2, Plenum Publishing Corporation, New York, NY, 1973.
[20] H. Ju, H. Meng, C.Y. Wang, Int. J. Heat Mass Transfer 48 (2005) 1303.
[21] A.A. Kulikovsky, J. Electrochem. Soc. 150 (2003) A1432.
[22] J.T. Hinatsu, M. Mizuhata, H. Takenaka, J. Electrochem. Soc. 141 (1994) 1493.
[23] Product Information, DuPont Nafion PFSA Membranes N-112, NE-1135, N-115, N-117, NE-1110 Perfluorosulfonic Acid Polymer, NAE101, 2004.
[24] Toray Carbon Paper Specification Sheet, Toray Industries Inc., Advanced Composites Department, Tokyo, 2001.